Effects of Cell Spatial Organization and Size Distribution on Ultrasound Backscattering

Ratan K. Saha and Michael C. Kolios

Abstract—In ultrasound tissue characterization dealing with cellular aggregates (such as tumors), it can be hypothesized that cell microstructure and spatial distribution dominate the backscatter signal. Effects of spatial organization and size distribution of nuclei in cell aggregates on ultrasound backscatter are examined in this work using 2-D computer simulations. The nuclei embedded in cytoplasm were assumed to be weak scatterers of incident ultrasound waves, and therefore multiple scattering could be neglected. The fluid sphere model was employed to obtain the scattering amplitude for each nucleus and the backscatter echo was generated by summing scattered signals originating from many nuclei. A Monte Carlo algorithm was implemented to generate realizations of cell aggregates. It was found that the integrated backscattering coefficient (IBSC) computed between 10 and 30 MHz increased by about 27 dB for a spatially random distribution of mono-disperse nuclei (radius = 4.5 μm) compared with that of a sample of periodically positioned mono-disperse nuclei. The IBSC also increased by nearly 7 dB (between 10 and 30 MHz) for a spatially random distribution of poly-disperse nuclei (mean radius ± SD = 4.5 ± 1.54 μm) compared with that of a spatially random distribution of mono-disperse nuclei. Two different Gaussian pulses with center frequencies 5 and 25 MHz were employed to study the backscatter envelope statistics. An 80% bandwidth was chosen for each case with approximately 0.32 mm as the full-width at half-maximum (FWHM) for the first pulse and 0.06 mm for the second. The incident beam was approximated as a Gaussian beam (FWHM = 2.11 and 1.05 mm for those pulses, respectively). The backscatter signal envelope histograms generally followed the Rayleigh distribution for mono-disperse and poly-disperse samples. However, for samples with partially ordered nuclei, if the irradiating pulse contained a frequency for which ultrasound wavelength and scatter periodicity became comparable ($d \sim \lambda/2$), then the histograms were better fitted by the Nakagami distribution. This study suggests that the shape of an envelope histogram depends upon the periodicity in the spatial organization of scatterers and bandwidth of the ultrasound pulse.

I. Introduction

STUDIES carried out mostly over the last few years used high-frequency (10 to 60 MHz) ultrasound to investigate backscattering properties of cell aggregates, which were used as simplified models of tumors [1]–[3]. In this regime, wavelengths (25 to 150 μm) approach the size (10 to 20 μm) of the cells or nuclei and exhibit much more

sensitivity to cell structure and changes in cell structure during cell death compared with the lower interrogating frequency range (<10 MHz) available with conventional ultrasound imagers [2]. This observation suggests that the high-frequency ultrasound backscattering technique can be used to detect cell apoptosis and also to monitor efficacy of cancer treatments [4], [5]. Although there are other more established methods that are used to detect apoptosis [for example, single photon emission CT (SPECT) and Positron emission tomography (PET)], ultrasonic detection of apoptosis has several distinct advantages. The ultrasound imaging method is nonionizing, less expensive (compared with SPECT, PET, etc.), easy to implement, and generally free from injection of foreign particles into the body before the exposure [6].

Kolios *et al.* [1] used an ultrasound spectral analysis method developed by Lizzi *et al.* [7] to analyze measured ultrasound signals from cell ensembles treated with chemotherapeutics and also from aggregates of healthy cells. They found that ultrasound backscatter intensity and spectral slope increased because of treatment and that was interpreted as a consequence of the decrease in effective scatterer size. Similarly, Vlad *et al.* [2] experimentally investigated how backscattering properties for several cell lines vary with time after radiotherapy, and consequently examined the potential of this technique to differentiate various types of cell death. Tunis *et al.* [3] studied the envelope statistics of ultrasound backscatter signals from cisplatin-treated aggregated acute myeloid leukemia (AML) cells and evaluated the applicability of various statistical distribution functions to model the envelope histograms. They reported that shape parameters of the generalized gamma distribution function were sensitive to the structural changes within cells induced by the drug. Oelze *et al.* [8] also used high-frequency ultrasound to differentiate and characterize rat mammary fibroadenomas and 4T1 mouse carcinomas. They generated quantitative ultrasound (QUS) images based on the estimated scatterer properties (e.g., average scatterer diameter, acoustic concentration, etc.). These properties were obtained by analyzing backscatter signals in the spectral domain and by employing a Gaussian form factor model [9]. They showed that QUS images are capable of distinguishing two types of tumors. In another investigation [10], the same group examined carcinoma and sarcoma in mouse models using QUS. It was observed that the estimated parameters extracted from the frequency band 10 to 25 MHz cannot distinguish between the two kinds of tumors, but those of 16 to 25 MHz can clearly show some differences.

Simulation studies have also been conducted to provide some insights into the interactions of waves with a collection of scatterers (cells or nuclei) and to examine the effects of spatial organization of scatterers and apoptotic changes in cell structure (caused by the nucleus condensation, fragmentation, and digestion) on ultrasound backscattering. For example, in a study, Hunt *et al.* [11] modeled each cell as a reflector located in its center and the resultant signal was calculated by using the linear superposition principle for the reflected signals from all the cells. Accordingly, the effects of the randomization of the spatial organization of cells on ultrasound backscatter were examined. The same group, to mimic nuclear condensation and fragmentation, assumed that each nucleus could be modeled as an ensemble of mini-scatterers and consequently the backscatter echo was constructed by following the same principle [12]. These studies showed that backscatter signal amplitude increased because of the randomization and condensation of nuclei. Thus, they were in agreement, qualitatively, with the experimental observations. However, the actual size, shape, and scattering aspects of particles were not taken into account. Moreover, no analysis was done to examine the effects of these parameters on the backscatter spectral characteristics or the envelope statistics.

The objective of the paper is to present a 2-D simulation study on the ultrasound backscattering properties of cell aggregates. This work uses a modified version of a theoretical model which has been extensively used to describe ultrasound backscattering by red blood cells [13]–[16]. In this work, nuclei embedded in cytoplasm were considered as weak scatterers of incident ultrasound waves (thus, multiple scattering was neglected). The scattering pattern was assumed to be given by the fluid sphere model for each nucleus and the resultant backscatter echo was generated by using linear superposition of scattered waves which originated from those nuclei. This model was recently employed by our group to compute ultrasound integrated backscatter for different cell lines treated with radiation therapy, as well as chemotherapy, and compared with those of viable cells [17]. A good correlation between the measured and simulated data was observed. The model has been used here to study the effects of the spatial organization and size distribution of scatterers on ultrasound backscatter for AML cell aggregates. A Monte Carlo simulation algorithm was employed to generate 2-D tissue realizations and, accordingly, both frequency-dependent backscattering coefficients and signal statistics were investigated. The Rayleigh and Nakagami distribution functions [18]–[20] were used to fit the envelope histograms, and consequently the distribution parameters were computed. Our results show that backscattering coefficient (BSC) generally increases with greater randomization of positions of scatterers as well as when the size dispersity increases. The backscatter signal envelope histograms generally follow the Rayleigh distribution. However, the Nakagami distribution provides good fits to the histograms when coherent components are present in the backscatter signals.
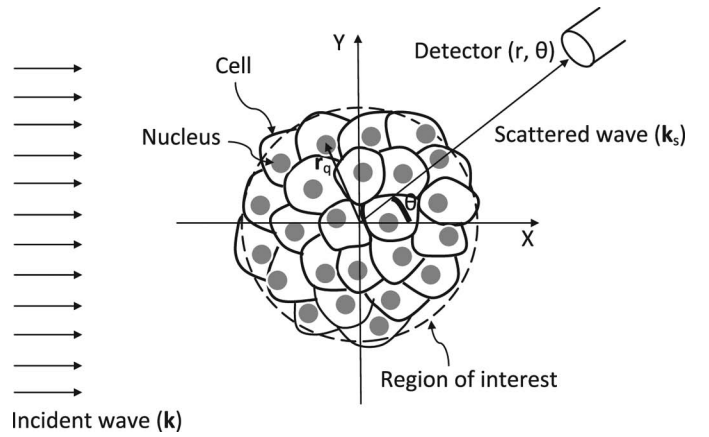
Fig. 1. Scattering diagram (top view). Here, $\mathbf{r}_q$ is the position vector of the qth scatterer with radius a_q and θ is the scattering angle. For backscattering, $\theta = \pi$.

The next section describes the theoretical model. In Section III, we illustrate the computer implementation scheme. The results obtained are presented in Section IV. The performance of the model presented here compared with other models and experimental results are discussed in Section V. Finally, we summarize our work in Section VI.

II. Theoretical Model

A. Derivation of the Backscattering Coefficient

The scattered field at a large distance r in the backscattering direction from the center of the scattering region comprising a collection of scatterers can be obtained by taking the linear superposition of scattered signals originating from the scatterers, and can be given by [9]

$$p_{\mathrm{s}}^{(1)}(\mathbf{r}) \approx \frac{e^{ikr}}{r} \sum_{q=1}^{N} \phi_{\mathrm{b}}(k, a_q) e^{i2\mathbf{k}\cdot\mathbf{r}_q}. \tag{1}$$

In this case, each scatterer produces a spherical wave because of its interaction with an incident plane wave and contributions from N scatterers distributed in the scattering region are summed up to obtain the resultant backscatter field in the asymptotic region. Eq. (1) is similar to [9, Eq. (4)]. Eq. (1) is based on the single-particle scattering theory, which is well established in the literature and has been used extensively to model ultrasound signals from various tissue samples [7], [9], [13]. Further, it is valid when scatterers are weak, and therefore multiple scattering can be neglected. In (1), ϕ_{b} represents the backscattering amplitude of an incident plane wave with wave vector $\mathbf{k}$ by the qth spherical scatterer with radius a_q and position vector $\mathbf{r}_q$. A scattering diagram is displayed in Fig. 1 to clarify the geometry and the notations. The subscripts b and s correspond to the backscattering and the scattered wave, respectively. Further, the superscript (1) indicates scattering of an incident plane wave. The exact analytical

solution (expression appears in [21, Eq. (8.2.15)]) for the backscattering amplitude of an incident plane wave with an amplitude equal to unity scattered by a fluid sphere can be written as [21]

$$\phi_{\mathrm{b}}(k,a) = \frac{i}{k}\sum_{l=0}^{\infty}(2l+1)b_l P_l(\pi), \qquad (2)$$

where

$$b_l = \frac{j_l'(x)j_l(y) - \alpha j_l(x)j_l'(y)}{h_l'(x)j_l(y) - \alpha h_l(x)j_l'(y)}, \qquad (3)$$

with $x = ka$, $y = nx$, $n = k_e/k = c/c_e$, $\alpha = n\rho/\rho_e$. Here, k and c are the wave number and speed of sound in the ambient medium; k_e and c_e are the same quantities for the scatterer. The notations j_l and h_l denote the spherical Bessel and Hankel functions of the order l, and prime indicates differentiation with respect to the argument. Further, P_l is a Legendre polynomial, which is a polynomial of degree l. The density of the surrounding medium and scatterer are designated by ρ and ρ_e, respectively. Note that both media (inside and outside the scatterer) have been considered as linear media. Thus, the frequency of the scattered wave is the same as that of the incident wave and that imposes the condition $ck = c_e k_e$. In general, ϕ_{b} is a complex quantity and, therefore, it retains the information of phase change associated with the scattering process. Moreover, this solution is valid over the entire frequency range (assuming no multiple scattering).

The differential backscattering cross-section per unit volume, or the BSC, is defined as the scattered power per unit solid angle per unit volume divided by the intensity of the incident wave, can be readily derived by using (1) as

$$\chi_{\mathrm{b}}(-2\mathbf{k}) = m\left\langle \frac{1}{N}\left|\sum_{q=1}^{N}e^{i2\mathbf{k}\cdot\mathbf{r}_q}\phi_{\mathrm{b}}(k,a_q)\right|^2\right\rangle, \qquad (4)$$

which is a general expression and can be used to compute the BSC for a poly-disperse system. Here, m is the number density of scatterers. The symbol $\langle\rangle$ denotes the ensemble average. It means that for a random system, quantitative estimation of an observable has to be made over many possible realizations to obtain a converging result. For a mono-disperse system, (4) simplifies to

$$\chi_{\mathrm{b}}(-2\mathbf{k}) = m\left\langle \frac{1}{N}\left|\sum_{q=1}^{N}e^{i2\mathbf{k}\cdot\mathbf{r}_q}\right|^2\right\rangle|\phi_{\mathrm{b}}(k,a)|^2 \qquad (5)$$
$$= mS(-2\mathbf{k})|\phi_{\mathrm{b}}(k,a)|^2.$$

The number density can be obtained by using the relationship $m = H/V_{\mathrm{s}}$, where H is the packing fraction of scatterers and V_{s} is the volume of a spherical scatterer. Here, $S(-2\mathbf{k})$ is the structure factor of the medium and dictates how backscattering would vary with spatial organization of mono-disperse scatterers. It can be written in terms of the Fourier transformation as [14], [16]

$$S(-2\mathbf{k}) = \left\langle \frac{1}{N}\left|\sum_{q=1}^{N}e^{i2\mathbf{k}\cdot\mathbf{r}_q}\right|^2\right\rangle = \left\langle \frac{1}{N}\left|\int N(\mathbf{r})e^{i2\mathbf{k}\cdot\mathbf{r}}\mathrm{d}\mathbf{r}\right|^2\right\rangle, \qquad (6)$$

where

$$N(\mathbf{r}) = \sum_{q=1}^{N}\delta(\mathbf{r}-\mathbf{r}_q), \qquad (7)$$

and referred to as the microscopic density function [14], [16]. An analog of (5) can be found in the literature dealing with ultrasound backscattering by red blood cells [13]–[16]. In the case of red blood cells, the Born approximation was used to determine the single-particle scattering amplitude and it worked accurately because the condition $ka < 1$ was always satisfied for incident waves with frequencies <40 MHz impinging on the red blood cells. However, the exact solution is valid over the entire frequency range and thus can be used even for situations where $ka > 1$. In this paper, we have computed (5) for different tissue samples and examined how backscattering would vary with the spatial organization of cells. We also computed (4) to study the effects of poly-dispersity on ultrasound backscattering.

In the low-frequency range, the structure factor can be approximated by the packing factor (W) of the suspension and thus, with this substitution, (5) reduces to

$$\chi_{\mathrm{b}}(-2\mathbf{k}) = mW|\phi_{\mathrm{b}}(k,a)|^2, \qquad (8)$$

and W is known as the Percus-Yevick packing factor [22], [23]. This theoretical model works well in the low-frequency range, where $ka < \pi/10$ (i.e., for Rayleigh scatterers) [13] and also for a spatially random distribution of non-overlapping scatterers with uniform size. In 2-D, for hard disks with equal radii, randomly distributed in space, W is related to the packing fraction as $W = (1 - H)^3/(1 + H)$. In 3-D, for spatially random distributions of impenetrable spheres with uniform size, W can be written as $W = (1 - H)^4/(1 + 2H)^2$. The frequency-dependent BSC predicted by (8) is calculated in this paper to compare with our simulation results and it is referred as PYPT (Percus-Yevick packing theory) in the following sections.

B. Derivation of the Backscatter Signal

The pressure field profile for a transducer with circular aperture in the far field regime can be approximated as

$$p_{\mathrm{in}}(x,y,z,t) \approx \left(\frac{1}{\pi\sigma_x^2}\right)^{1/4}\exp\left(-\frac{y^2}{2\sigma_y^2}\right)\exp\left(-\frac{z^2}{2\sigma_z^2}\right)$$
$$\times\exp\left(-\frac{(x-ct)^2}{2\sigma_x^2}\right)e^{ik_0(x-ct)}, \qquad (9)$$

where σ_x is related to the pulse width of the input pressure pulse and σ_y, σ_z define the beam widths along two lateral directions. The center frequency (f_0) of the pulse

is related to k_0 as $2\pi f_0 = ck_0$. It models a Gaussian beam and also a Gaussian modulated pulse propagating along the positive x-axis. This modeling approach has been used previously in the context of ultrasound backscattering by a tissue medium [12], [24], [25]. In general, because of the frequency-dependent diffraction, the incident pressure field amplitude profiles along the transverse directions of wave propagation would differ for different frequency waves emitted by a transducer. This has not been considered in (9), meaning that the beam widths along the lateral directions would be same for all frequencies that are contained in the pulse. However, this simple model is useful because essential aspects of a backscatter signal are greatly defined by the interference of backscatter waves generated by a collection of scatters distributed in space. At $t = 0$, the incident pulse can be written as

$$
p_{\text{in}}(x,y,z,0) \approx \left(\frac{1}{\pi\sigma_x^2}\right)^{1/4} \exp\left(-\frac{y^2}{2\sigma_y^2}\right)\exp\left(-\frac{z^2}{2\sigma_z^2}\right) \\ \times \exp\left(-\frac{x^2}{2\sigma_x^2}\right)e^{ik_0 x}, \tag{10}
$$

which means that the pulse is centered at $x = 0$. The spatial Fourier transformation of (10) provides the frequency content of the incident pulse, and thus one obtains

$$
\tilde{p}_{\text{in}}(k,y,z) \approx \exp\left(-\frac{y^2}{2\sigma_y^2}\right)\exp\left(-\frac{z^2}{2\sigma_z^2}\right)\mathcal{F}(k), \tag{11}
$$

where

$$
\mathcal{F}(k) = \left(\frac{1}{\pi\sigma_k^2}\right)^{1/4}\exp\left(-\frac{(k-k_0)^2}{2\sigma_k^2}\right), \tag{12}
$$

and $\sigma_k = 1/\sigma_x$. The backscatter pressure in the asymptotic $(r \to \infty)$ region for 3-D spatial distributions of scatterers can be obtained by using the linear superposition of scattered waves, and hence it becomes [26]

$$
p_s^{(2)}(r,t) \approx \frac{1}{\sqrt{2\pi}}\int \mathrm{d}k \frac{e^{ik(r-ct)}}{r} \\ \times \left[\sum_{q=1}^{N}\exp\left(-\frac{y_q^2}{2\sigma_y^2}\right)\exp\left(-\frac{z_q^2}{2\sigma_z^2}\right)\mathcal{F}(k)\phi_{\text{b}}(k,a_q)e^{i2kx_q}\right], \tag{13}
$$

and for 2-D spatial distributions of scatterers, it can be written as

$$
p_s^{(2)}(r,t) \approx \frac{1}{\sqrt{2\pi}}\int \mathrm{d}k \frac{e^{ik(r-ct)}}{r} \\ \times \mathcal{F}(k)\left[\sum_{q=1}^{N}\exp\left(-\frac{y_q^2}{2\sigma_y^2}\right)\phi_{\text{b}}(k,a_q)e^{i2kx_q}\right]. \tag{14}
$$

Note that in this case, the function ϕ_{b} is properly weighted by the magnitudes of incident pressure field at the positions of the scatterers. Eq. (13) has been derived from [26,

Eq. (7)] by incorporating scattering of an incident Gaussian pulse with a Gaussian beam profile by many particles. The superscript (2) indicates scattering of a pulse. These expressions can be used to obtain the backscatter pressure at each time point at the position of observation for a tissue sample when insonified by a pulse of interest. Note that the corresponding backscatter pressure would be a complex quantity. However, the backscatter signal (referred to as the RF signal in the later sections) can be generated from the real parts of backscatter pressure time-series data and the signal envelope can be determined accordingly from the magnitudes.

The SNR, defined as the mean divided by the standard deviation of an envelope, can be determined from the envelope of an RF signal's time-series data. The RF envelope histograms can be fitted with different probability distribution functions such as the Rayleigh and Nakagami probability distributions [18]–[20] to characterize a tissue sample. The Rayleigh probability density function is given by [18]

$$
f(A) = \frac{A}{\sigma^2}\exp\left(-\frac{A^2}{2\sigma^2}\right), \quad A \geq 0; \quad \sigma > 0, \tag{15}
$$

where σ is the scale parameter and $2\sigma^2$ is the mean intensity of the Rayleigh distribution. The Rayleigh distribution arises when the scattering region contains a large number of randomly distributed identical scatterers with no coherent signal component [19], [20]. The Nakagami probability density function is expressed as [18]–[20]

$$
f(A) = \frac{2\beta^\beta A^{2\beta-1}}{\Gamma(\beta)\Omega^\beta}\exp\left(-\frac{\beta A^2}{\Omega}\right), \quad A \geq 0; \quad \beta, \Omega > 0. \tag{16}
$$

Here, Ω and β are the scale and shape parameters, respectively, and Γ is the gamma function. Further, Ω and $\sqrt{\beta}$ are the mean intensity and intensity SNR of the Nakagami distribution, respectively. Note that the symbol β is used here to denote the letter m of [18, Eq. (4)]. The Rayleigh distribution is a special case of the Nakagami distribution (with $\beta = 1$). The Nakagami distribution is a simple two-parameter distribution function [18]. It is applicable to describe the statistics of the backscatter echo envelopes for tissues containing a collection of scatterers with varying number densities, varying scattering strengths, and in the absence or presence of coherent signals [18].

Another distribution, namely the generalized gamma distribution, was also employed to characterize ultrasound backscatter signals [3], [19]. It may also be noted that the generalized gamma distribution has been introduced independently in the equivalent form of the generalized Nakagami distribution in [27]. Recently, an improved parameter estimation algorithm for the homodyned K-distribution was developed and tissue parameters (e.g., number of scatterers per resolution cell and ratio of coherent to incoherent backscatter signal energy) were obtained subsequently using those estimates [28]. However, the gener-

alized gamma and homodyned K-distributions were not used in this study because the simpler Nakagami distribution provided good fits to the envelope histograms. For comparison with a widely used distribution, the Rayleigh distribution results were also included.

III. Simulation Methods

A. Choice of the Scattering Region

A 2-D simulation study was performed to investigate the effects of cell spatial organization and size distribution on ultrasound backscattering. 2-D simulations are computationally less expensive than 3-D simulations. However, sufficient insights can be gained regarding the interactions of ultrasound waves with a collection of densely packed scatterers (e.g., present in a cell aggregate) [14], [17]. In addition to that, physically meaningful results can be obtained by executing 2-D simulations [17], [25]. It can also be noted that 2-D sections can provide quantitative information of 3-D structure if the basic isotropy conditions are satisfied and that has been showed in detail in [29]. Therefore, in this study, (4) and (5) were computed for 2-D simulated realizations and compared with that of (8) using the 2-D packing factor. Similarly, backscatter signals were simulated for 2-D samples by implementing (14).

In this study, we fixed our region of interest (scattering region) as 1000×1000 μm. It is hypothesized that a region completely filled with cells mimics the tight cell packing that is the characteristic of many xenograft tumors. In such an aggregate, it is hypothesized that the cytoplasm [30] acts as the ambient medium and the nuclei behave as main scattering centers because their acoustic properties are different from those of cytoplasm. The nucleus-to-cell volume ratio for AML cells has been measured to be ≈55% [30] and therefore nuclei would occupy ≈55% of the total volume in an AML cell aggregate (3-D sample). This packing fraction may not be attained sometimes in 2-D because the maximum possible area packing in 2-D by discs with equal radii is 0.5472 ± 0.0002 for random loose pack configurations [31]. In this study, we used a 50.36% packing fraction by the nuclei.

B. Scatterer Properties

The radius of a nucleus was taken as $a = 4.5$ μm [30]. Accordingly, the total number of nuclei in this simulation was 7921 (= 89×89). The density and sound velocity within the nucleus were chosen as $\rho_e = 1180$ kg/m^3 and $c_e = 1523$ m/s, respectively [32]. These numerical values are close to the estimated values for the OCI-AML-5 cells presented in a recent paper by our group [33]. In these studies [32], [33], cell acoustic properties were estimated by optimizing the experimental backscatter spectral data and the theoretical model presented in (2). Corresponding quantities of the surrounding medium (saline water) were taken as $\rho = 1000$ kg/m^3 and $c = 1483$ m/s, respectively

[32]. These values were used to compute the single-particle backscattering amplitude [see (2)].

C. Computation of the Backscattering Coefficient

To study the effect of spatial organization on the backscattering, we considered four different tissue samples. In case of the first tissue sample (denoted Regular), the scatterers were placed at regular positions with a separation of $d = 11.23$ μm, forming a perfect lattice structure [Fig. 2(a)]. The separation became fixed from the fact that scatterers were placed regularly within the region of interest forming a square lattice under the periodic boundary conditions. The frequency dependent BSC was determined subsequently. For the second sample (denoted Mixture1), a mixture of regularly placed nuclei (51.71% of the total number of nuclei) and randomly placed nuclei (48.29% of the total number of nuclei) was used [Fig. 2(b)]. This particular numerical value (51.71%) was chosen for regularly aligned nuclei because that provided a square number (4096 = 64×64) for the scatterers allowing the generation of a square lattice under the periodic boundary conditions within the region of interest. The random positions of scatterers were generated by using the random sequential adsorption (RSA) algorithm [34]. In this method, coordinates for a particle were proposed and accepted if the particle did not overlap with already situated particles under periodic boundary conditions. Otherwise the trial move was canceled and a new move was initiated. The same procedure was repeated for all other particles to assign their coordinates. Once the initial arrangement was achieved, the tissue sample was evolved (using random shuffling of randomly positioned particles) to simulate new configurations to obtain the ensemble average of the BSC. This strategy was also followed to generate the spatial organization of the nuclei for the third sample [denoted Mixture2, Fig. 2(c)]. In this case, 25.64% nuclei were periodically placed and the remaining nuclei occupied random positions. For the fourth sample (denoted Random), all of the nuclei were positioned randomly in the region of interest by using the RSA technique [Fig. 2(d)]. Consequently, the ensemble average of BSC was determined over a large number of realizations. For each tissue sample, 20 simulations were executed in a remote computer cluster to obtain the mean BSC. In addition, to characterize the spatial distributions of nuclei of these samples, we computed the pair correlation function $g(r)$ [35]. In two dimensions, it is defined as the number of particles within an annular area between r and $r + dr$ from the center of the reference particle divided by the product of total number of particles, area of the annular region, and the average number of particles per unit area. The pair correlation function can provide a measure of structure that is present in a collection of particles.

The effects of size dispersity on ultrasound backscattering were also studied in this work. In this case, we considered three different tissue samples. The first prototype contains randomly placed mono-disperse nuclei
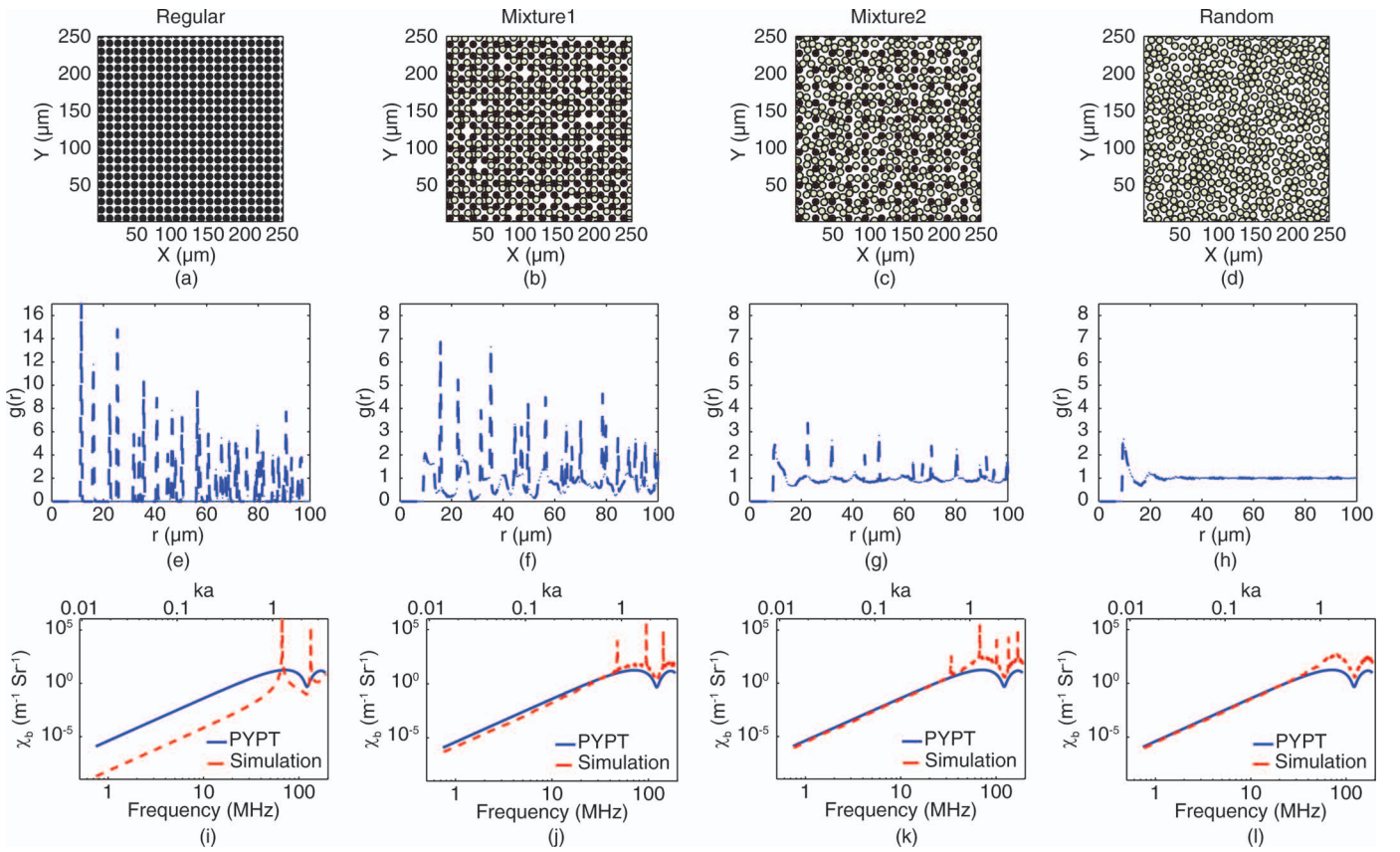
Fig. 2. (a) A tissue sample with regularly spaced nuclei. (b) and (c) Tissue samples with mixtures of regularly (dark circles) and randomly placed nuclei (gray circles). (d) A configuration of randomly packed nuclei. (e)–(h) Plot of pair correlation function for (a)–(d), respectively. (i)–(l) Frequency-dependent BSC for (a)–(d), respectively.

and defined as mono-disperse in the text [Fig. 3(a)]. This is exactly the same as the sample Random in the previous case. The second [denoted Poly-disperse1, Fig. 3(b)] and third [denoted Poly-disperse2, Fig. 3(c)] samples contained scatterers with different size distributions. In both cases, it was assumed that the total area occupied by the nuclei (therefore, the packing fraction) remained similar to that of the mono-disperse sample. The size distribution of the nuclei followed a Gaussian distribution for each poly-disperse sample. The mean radius was the same (4.5 μm) for both cases. The numerical values of standard deviation of the particle size distribution were chosen as 0.99 and 1.54 μm for Poly-disperse1 and Poly-disperse2, respectively. The spatial distributions of nuclei were generated by using the RSA method. However, in these cases, the nuclei positioning algorithm started with the largest nuclei and all the nuclei with largest size were placed first. The smaller nuclei were chosen subsequently and the same procedure was repeated [36]. For these two new samples, mean BSCs were computed and compared with the first sample. This allowed the examination of the effect of different size distributions on ultrasound backscattering.

D. Computation of the Backscatter Signal

To investigate how the backscattering signal envelope statistics depend on the spatial organization and size distribution of scatterers, a Gaussian pulse was employed. Two different pulses were considered. The center frequency of the first pulse was 5 MHz and that of the second pulse was 25 MHz. The first pulse was chosen to match the frequency of clinical transducers, which usually operate in this range. The second one was chosen because in many experiments from our group, the 10 to 30 MHz frequency range was used to achieve better resolution and sensitivity (to capture subtle cellular structural changes induced by the therapies). An 80% bandwidth was used for both pulses. Accordingly, the numerical value of σ_x was calculated to be 0.137 mm for the first pulse and 0.027 mm for the second. The corresponding numerical values for the full-width at half-maximum (FWHM) could be computed to be nearly 0.322 and 0.065 mm, respectively. The beam widths of those pulses were chosen to be fixed as $\sigma_y = 0.89$ and 0.45 mm, respectively. That provided the FWHMs as 2.11 and 1.05 mm for those incident beams, respectively. Similar values could be found for some commercially available transducers (e.g., the Panametrics Videoscan series [37]). The size of the resolution cell using these FWHM values could be estimated to be approximately 0.679 mm^2 and 0.068 mm^2 for two cases, respectively. Therefore, the scatterer density became nearly 5375 scatterers/resolution cell for the first pulse (for the mono-disperse nuclei with a = 4.5 μm and 50.36% area packing fraction). This value for the same sample was about 538 scatterers/resolution
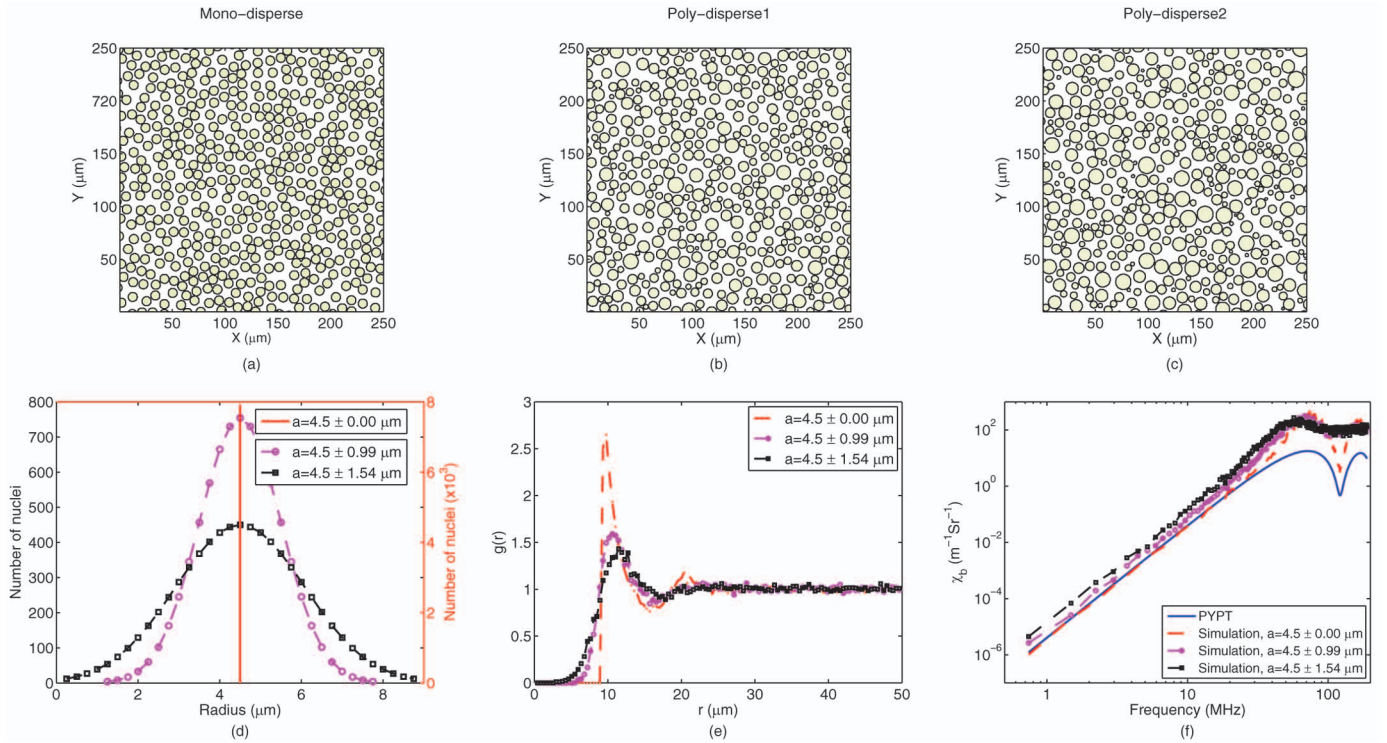
Fig. 3. (a) A random arrangement of mono-disperse nuclei. (b) and (c) are the same as (a) but for poly-disperse nuclei. (d) Variations of number of nuclei with radius for mono-disperse (solid line, right axis) and poly-disperse samples (broken lines, left axis). The mean (± 1 standard deviation) values are given in the legends. (e) Plots of pair correlation function for three samples. (f) Variations of frequency-dependent BSCs for those samples.

cell for the second pulse. For this study, we chose a bigger region of interest, 4000×4000 µm. Therefore, for a mono-disperse sample, the number of particles became $N = 126\,736$. We followed the same steps as those previously described to achieve a configuration with a non-overlapping spatial distribution of scatterers. A bigger region of interest provided a sufficiently long RF line and was long enough to perform meaningful envelope statistics analysis. Further, it would increase the resolution in the frequency domain and that was required for accurate estimation of a scattered signal through numerical integration as given in (14). For regularly packed cells, a single RF line was generated, and subsequently the histogram of the signal was obtained. It did not contain randomly located particles, so only one characteristic RF line could be obtained. On the other hand, for the other tissue samples, 100 different lines were generated to study the envelope statistics for those signals. Similarly, signal statistics were also studied for each poly-disperse tissue sample. The SNR (defined previously as the ratio of mean to standard deviation of the RF envelope) and the envelope histogram were obtained for each tissue sample from those 100 RF lines. The Rayleigh and Nakagami probability distribution functions were employed to fit an envelope histogram and the fit parameters were estimated using different-order moments of the envelope data as given in [18]–[20]. The error associated with the best fit was also computed to evaluate the performance of a distribution function. The error (Δ) was estimated by defining $\Delta = \sum_{i=1}^{31}(o_i - e_i)^2$, where o_i and e_i are

observed and expected values. The index i ran from 1 to 31 because a bin size of 31 was used in this study.

IV. SIMULATION RESULTS

A. Analysis of the Backscattering Coefficient

1) The Effect of Spatial Organization: An arrangement of nuclei at regular positions is shown in Fig. 2(a). For clarity, we have presented a smaller portion (250×250 µm) of the whole region of interest (1000×1000 µm). Figs. 2(b) and (c) represent tissue realizations for mixtures of periodically (dark circles) and randomly located nuclei (gray circles). Fig. 2(d) illustrates a completely random packing of nuclei. The variation of $g(r)$ is shown in the second row of Fig. 2 for those tissue samples. The spikes in the pair correlation function plot in Fig. 2(e) illustrate that there is a large amount of order in the system. Particles can only be found at some distinct separations, as given by the locations of the peaks on the x-axis. Fig. 2(f) demonstrates that the medium (Mixture1) is composed of periodic and random distributions of particles. The decrease in the height of the sharp spikes indicates that there is still some degree of orderliness in the system. However, nonzero values of $g(r)$ for all other separations confirm that the system contains randomly distributed nuclei too. Fig. 2(g) (for Mixture2) is similar to Fig. 2(f) but the heights of the peaks have further decreased in this case.

TABLE I. VARIATIONS OF THE INTEGRATED BACKSCATTERING COEFFICIENT (IBSC) AND SPECTRAL SLOPE (SS) FOR DIFFERENT TISSUE SAMPLES.

	Regular	Mixture1	Mixture2	Random/ Mono-disperse	Poly-disperse1	Poly-disperse2
IBSC $(m^{-1} \cdot Sr^{-1})$	0.0020	0.5957	0.7597	0.9685	2.0675	4.8471
IBSC (dB)	−26.82	−2.11	−1.05	0	3.29	6.99
SS	4.36	4.38	4.20	4.17	4.26	4.47

The IBSC and SS were determined between 10 and 30 MHz for each sample.

Moreover, the probability of finding particles separated by other distances has increased and oscillates around 1. Fig. 2(h) shows that at a large distance, $r > 5a$, $g(r)$ becomes 1. This indicates that there is a uniform probability of finding other particles at large distances from the center of the reference particle. Therefore, no specific structure lies in the system for $r > 5a$.

In Fig. 2(i), the variation of BSC with frequency is plotted for the ordered tissue. For comparison, BSC predictions by the Perucs-Yevick packing theory are also included in the same graph (solid line). The variation of the size parameter (ka) in this frequency range is also shown along the top axis in the same figure. The BSC is generally significantly lower than that of the PYPT because the PYPT is valid for spatially random distribution of non-overlapping particles with uniform size. However, sharp peaks are observed when the scatterer separation d becomes integer multiples of $\lambda/2$. Here, d (11.23 µm) denotes the nearest neighbor distance and λ refers to the incident wavelength. For these conditions, scattered signals interfere constructively, leading to strong backscatter echoes. Fig. 2(j) shows the variation of BSC with frequency for Mixture1. The backscatter curve retains sharp spikes because of the periodicity of some particles. The randomization of the other particles causes an increase in the BSC in the low-frequency range. However, differences between simulated results and that of PYPT arise from the fact that some of the particles are regularly positioned for this sample and, hence, it is not a spatially random distribution of scatterers. Similar observations can also be made from Fig. 2(k), which plots the variation of BSC for Mixture2. In this case, the BSC has increased even more in the low-frequency range and has become almost comparable to the Percus-Yevick line. In Fig. 2(l), the plot illustrates how backscattering varies with frequency when the sample contains randomly distributed nuclei. The simulation results exactly match the PYPT results up to 16 MHz, where $ka < \pi/10$ and the PYPT assumptions remain valid. This agreement in the low-frequency range also validates the computer code developed for this work. The curves separate after 16 MHz and become greater, with the greatest differences at the positions of maxima because the PYPT is not valid when $ka > \pi/10$.

The integrated backscattering coefficient (IBSC), defined by

$$\text{IBSC} = \frac{1}{(k_2 - k_1)} \int_{k_1}^{k_2} \chi_{\text{b}}(k) \mathrm{d}k, \qquad (17)$$

and spectral slope have also been computed between 10 and 30 MHz, before the spikes in the BSC occur. Note that spectral slope is related to the frequency dependence of the BSC. It can be determined from the slope of a BSC curve, where it exhibits linear variation with incident frequency in a log-log scale. The estimated values are presented in Table I. As the randomization increased, the IBSC also increased and is maximal for the Random system. The IBSC for the sample Regular is about 27 dB less than that of the Random. The variation of spectral slopes is also shown in Table I. The spectral slope decreased from 4.36 for Regular to 4.17 for Random, showing that the spectral slope is not strongly dependent on spatial positioning of scatterers. It may also be noted that the spectral slope for the sample Random is about 4 (data not shown) up to 16 MHz, where the scatterers behave as the Rayleigh scatterers. However, the spectral slope for the same sample in the frequency range 10 to 30 MHz is greater than 4, because in this case scatterers cannot be considered as Rayleigh scatterers and backscattering is described by (2) for fluid spheres.

2) The Effect of Size Distribution: Three representative configurations of randomly placed nuclei with varying size distributions are shown in Figs. 3(a)–3(c). The corresponding size distribution histograms are plotted in Fig. 3(d). The Mono-disperse sample is composed of scatterers (number of scatterers = 7921) with uniform size [the Mono-disperse population is represented by the solid line and the right y-axis in Fig. 3(d)] but the size distributions for Poly-disperse1 and Poly-disperse2 follow Gaussian distributions [broken lines and left y-axis in Fig. 3(d)]. The mean radius (4.5 µm) and the total area occupied by the nuclei remained constant for all samples. The variations of pair correlation functions are given in Fig. 3(e). No two particles were found at a separation <9 µm for the Mono-disperse sample. However, for the poly-disperse samples, particles can be found at a separation <9 µm because of the presence of smaller particles in the samples. Moreover, at a distance >25 µm, the structural properties of all samples become similar. Frequency-dependent BSCs are plotted in Fig. 3(f). In this figure, simulation results for the sample Mono-disperse show excellent agreement with that of PYPT up to 16 MHz, where $ka < \pi/10$. However, simulated BSC curves for Poly-disperse1 and Poly-disperse2 would not match with that of the PYPT because they contain scatterers with size distributions. It is evident from this figure that the BSC increased as the

TABLE II. Variations of the SNR, Rayleigh (R) and Nakagami (N) Parameters for Different Tissue Samples for an Incident Pulse With 5 MHz Center Frequency.

		Regular	Mixture1	Mixture2	Random/ Mono-disperse	Poly-disperse1	Poly-disperse2
SNR		0.26	1.93	1.73	1.73	1.85	1.94
R fitting	σ	9.83e−8	1.94e−6	2.28e−6	2.60e−6	3.59e−6	5.31e−6
	Δ_R	758.93	36.46	60.55	65.07	36.69	41.93
N fitting	Ω	5.89e−15	7.58e−12	1.05e−11	1.36e−11	2.58e−11	5.67e−11
	β	0.46	0.97	0.96	0.96	0.98	0.98
	Δ_N	83.79	33.03	53.77	56.40	35.03	40.04

Associated error (Δ) of each fitted curve is also presented. The subscripts R and N indicate the Rayleigh and Nakagami distributions, respectively.

TABLE III. Variations of the SNR, Rayleigh (R) and Nakagami (N) Parameters for Different Tissue Samples for an Incident Pulse With 25 MHz Center Frequency.

		Regular	Mixture1	Mixture2	Random/ Mono-disperse	Poly-disperse1	Poly-disperse2
SNR		0.13	1.85	3.08	1.82	1.89	1.90
R fitting	σ	3.77e−6	5.13e−5	1.06e−4	4.98e−5	8.41e−5	12.81e−5
	Δ_R	639.42	22.44	519.00	16.17	15.34	16.40
N fitting	Ω	7.91e−12	5.25e−9	2.02e−8	4.96e−9	1.42e−8	3.29e−8
	β	0.54	1.02	2.71	0.99	0.99	0.98
	Δ_N	16.37	16.17	56.89	16.08	14.76	13.54

Associated error (Δ) of each fitted curve is also presented. The subscripts R and N indicate the Rayleigh and Nakagami distributions, respectively.

standard deviation of size distribution increased. The increase in BSC is distinctively clear up to 30 MHz but after that, differences between the curves become less obvious. Moreover, at higher frequencies (>80 MHz), instead of oscillatory patterns in the frequency dependence, smoother variations of BSCs are obtained for the poly-disperse media. This is because the positions of spectral resonances are different for different nuclear sizes, and that results in smaller fluctuations. The numerical values of IBSCs and spectral slopes are tabulated in the last three columns of Table I. Both IBSC and spectral slope increased as the dispersity increased. The IBSC increased by about 3 dB and 7 dB for the Poly-disperse1 and Poly-disperse2 samples, respectively, when compared with the Mono-disperse sample. The spectral slope increased from 4.17 to 4.47.

B. Analysis of the Backscatter Signal

1) The Effect of Spatial Organization: The scattered signals were obtained by evaluating (14) for different pulses and tissue samples. The backscatter signal from the regularly arranged nuclei is given in Fig. 4(a) for an incident pulse with 5 MHz center frequency. Apart from the two edges, the signal amplitude is small in the central region and this is due to destructive interference of scattered signals. The signal amplitude gradually increases as the organization of nuclei becomes more random, as shown in Figs. 4(b) and 4(c). It reaches the maximum for a completely random packing of nuclei, as displayed in Fig. 4(d). The corresponding histograms generated from envelopes of the signals are shown in Figs. 4(e)–4(h). The histograms were generated from 100 RF lines obtained from 100 different realizations and accordingly fitted with the Rayleigh and Nakagami distribution functions. The numerical

values of the SNR of the echo envelopes and estimations of parameters of these two distributions are presented in Table II. The SNR for the first sample is smaller than 1.91, denoting a pre-Rayleigh regime. The histogram was more accurately fitted by the Nakagami distribution and the error was comparatively small [Fig. 4(e) and Table II]. For other samples, the SNR varied between 1.73 to 1.93, as given in Table II. The Rayleigh distribution function provided reasonably good fits to the histograms but the Nakagami distribution was marginally better for each case. The error associated with the Nakagami fitting was smaller than that of the Rayleigh for each sample (Table II). It is also clear from Table II and from Figs. 4(e)–4(h) that the Rayleigh fit parameter σ increased gradually as the sample moved from completely ordered packing to disordered packing. The Nakagami parameter Ω also showed the same trend. This is not surprising because $2\sigma^2$ of the Rayleigh distribution corresponds to Ω of the Nakagami distribution because both represent the mean intensity. The β parameter of this distribution remained close to 1 (reconfirming why the Rayleigh distribution provided good fits to the histograms).

The signal statistics for a pulse with a 25 MHz center frequency have been studied and estimates of the parameters are displayed in Table III. The backscatter signal from the first sample (Regular) looked similar to that of the 5-MHz pulse [Fig. 4(a)]. The backscatter signal envelope histograms for Mixture1 and Random also followed the Rayleigh distribution for this input pulse. The difference of σ for Mixture1 and Random is not significant, as it was in case of the 5-MHz pulse. The Nakagami distribution also provided similar fits to the histograms and corresponding numerical values of the Nakagami shape parameter (β) found to be close to 1. The fitting errors of
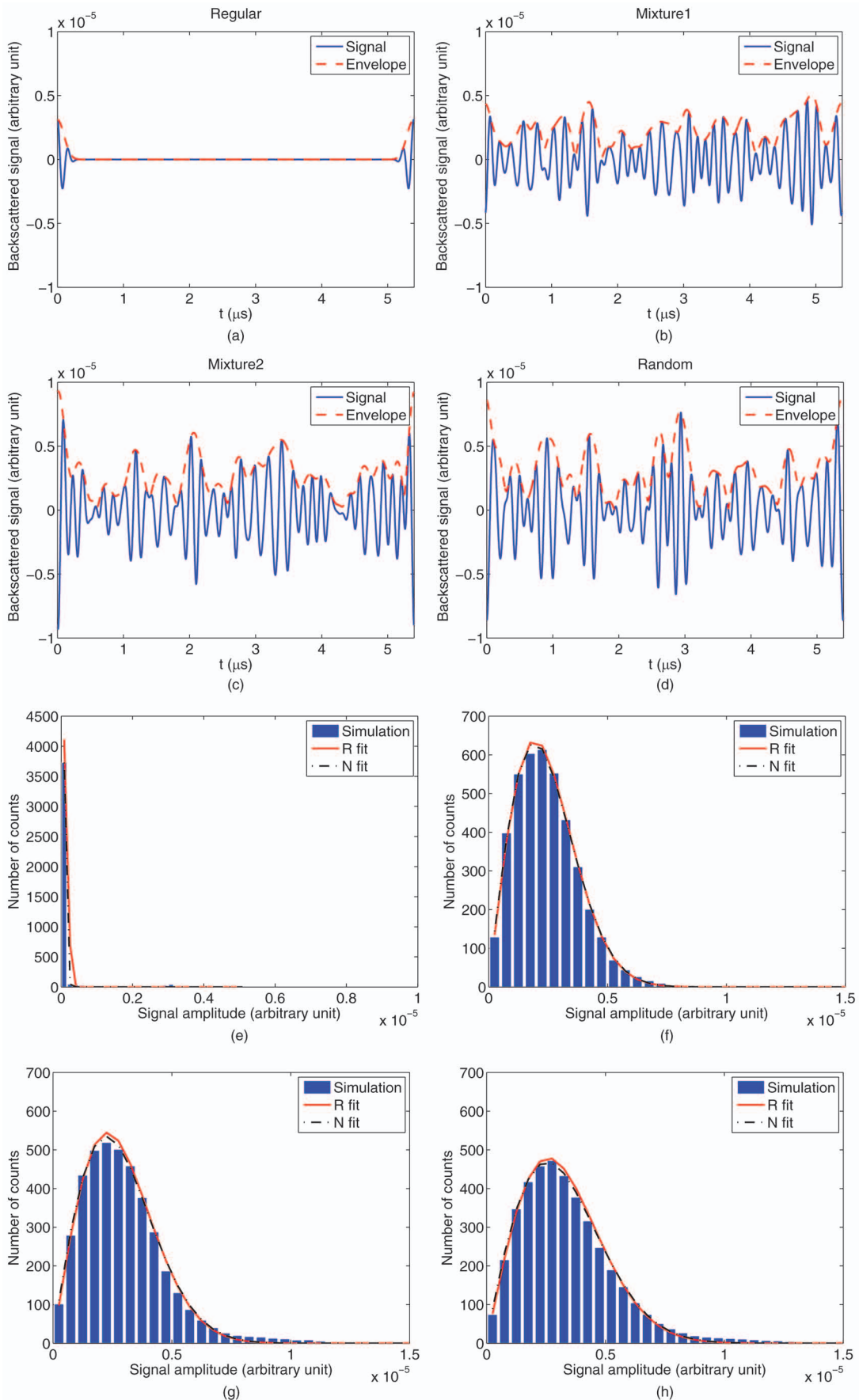
Fig. 4. (a)–(d) Representative signals from four different tissue samples. (e)–(h) Corresponding histograms for 100 RF lines and fitted with Rayleigh (R) and Nakagami (N) distribution functions.
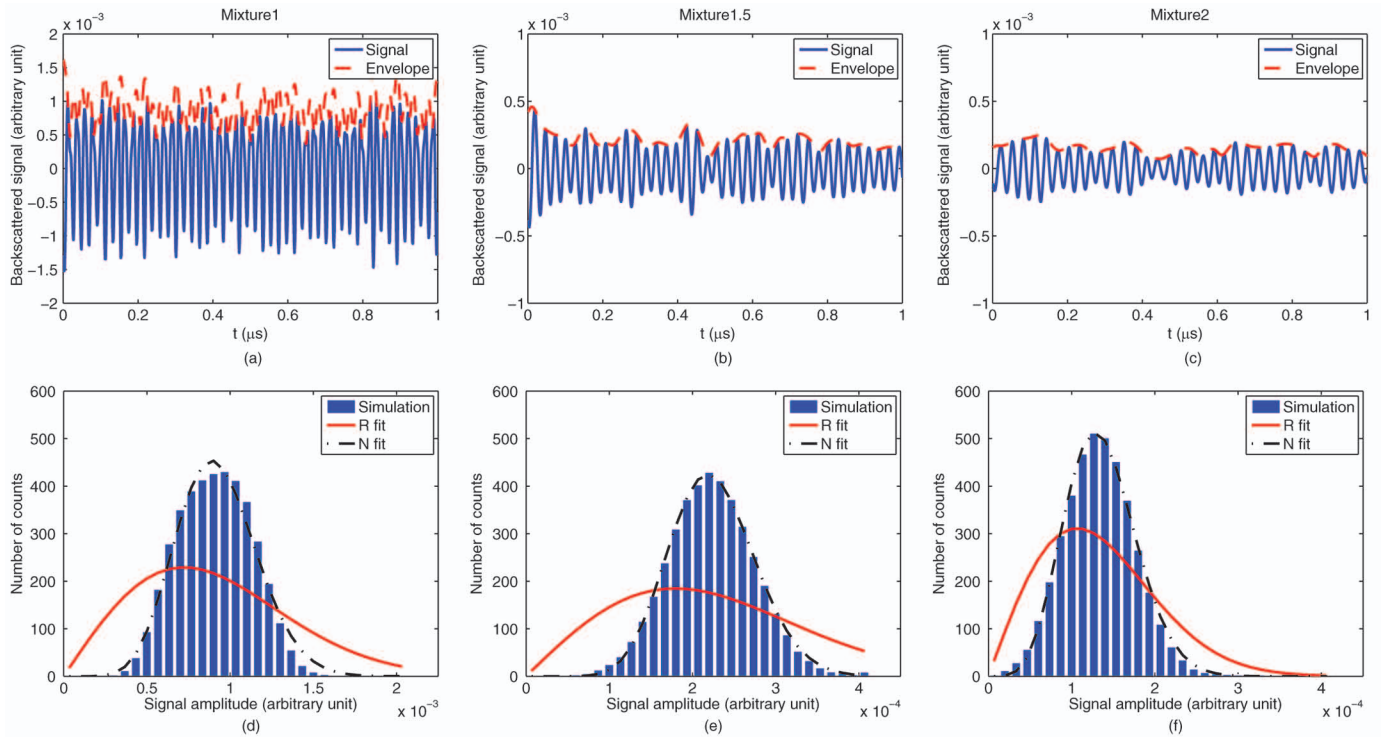
Fig. 5. (a)–(c) Simulated signals for Mixture1 (excited with 50-MHz pulse), Mixture1.5 (excited with 25-MHz pulse), and Mixture2 (excited with 25-MHz pulse). For clarity, a portion of the RF line is presented for each sample. (d)–(f) Corresponding histograms generated from 100 RF lines fitted with the Rayleigh (R) and Nakagami (N) distribution functions.

these distributions are comparable (Table III). Mixture2 contained some regularly placed nuclei with periodicity $d = 22.22$ μm, and at the same time the incident pulse contained a frequency (33.37 MHz) for which the condition $d \sim \lambda/2$ was satisfied. For this case, the histogram did not follow the Rayleigh distribution [see Fig. 5(f)] and the corresponding fitting error was also large (see Table III). The SNR is larger than 1.91, indicating a post-Rayleigh regime. The Nakagami distribution function exhibited much better fit to the histogram [see Fig. 5(f)] and the associated fitting error was small (see Table III). The shape parameter of this distribution also showed large variation compared with other samples meaning that the Rayleigh distribution would not be able to capture the envelope characteristics for that sample when probed with such a pulse.

To study the effect of periodicity of scattering structures on the signal statistics in detail, along with Mixture2, we also considered two more cases. In the first case, we insonified Mixture1 with a 50-MHz pulse. In the second case, we generated another sample (Mixture1.5, for which 31.56% of the particles were regularly placed and the remaining nuclei were randomly positioned) and irradiated by a 25-MHz pulse. In both cases, it was ensured that there was a frequency within the bandwidth of the pulse for which the wavelength was on the order of the nuclei periodicity. Representative RF lines for such samples are displayed in Figs. 5(a)–5(c). For clarity of the figure, a smaller portion is presented for each sample. It can be

seen that signal envelope amplitude increased and its fluctuation reduced significantly (compared with those of Fig. 4) because of the presence of coherent signals generated from periodically aligned scatterers. As a result, the SNR also became greater than 1.91 for each sample. The corresponding histograms are shown in Figs. 5(d)–5(f). The Nakagami distribution function provided much better fits to these histograms than the Rayleigh distribution. In fact, the Rayleigh distribution function is not useful in this case. The shape parameter of the Nakagami distribution was always computed to be more than 1 (data not shown), which suggests large deviations from the Rayleigh distribution.

2) The Effect of Size Distribution: Signal statistics of samples composed of different size distributions of nuclei were also studied. Numerical values of the estimated parameters are given in the last three columns of Table II for the 5-MHz pulse and in Table III for the 25-MHz pulse. It can be observed from Table II and Table III that the SNR increased as the size dispersity increased and it is close to 1.91 for Polydisperse2. Furthermore, σ and Ω increased as the dispersity increased and doubled compared with the mono-disperse sample for both pulses (at the highest level of dispersity). The numerical values of β remained very close to 1 for these samples. The fitting characteristics of the Rayleigh distribution are similar to that of the Nakagami distribution because errors of the fitted curves generated from these distributions are nearly the same for each sample.

V. Discussion

A. Backscattering Coefficient Results

In an earlier study, Hunt *et al.* [11] showed that greater randomization of positions of scatterers resulted in higher backscatter signal strength. This is also confirmed in the present study (Fig. 2 and Table I). The IBSC increased as the number of particles with random positions within the sample increased. For instance, the IBSC increased by about 27 dB for the sample containing randomly located scatterers compared with that of orderly packed sample. The spectral slope did not change significantly in this frequency range, 10 to 30 MHz, where ka varied between 0.19 and 0.57. Note that the spectral slope for the sample with randomly distributed scatterers is marginally higher ($\approx 4\%$) than that of the Rayleigh scatterers for which $ka < \pi/10$ [13]. For a sample with fully or partially ordered scatterers, the heights and positions of the peaks of the BSC curve determine the magnitude of the spectral slope. Note that the heights of the peaks of a BSC curve depend upon the proportion of regularly placed particles. The positions of the peaks of a BSC curve along the frequency axis are dependent upon the periodicity of regularly separated particles. For example, the spectral slope is greater in the sample Regular because of the appearance of a strong peak at 66 MHz in Fig. 2(i). However, for Mixture1 and Mixture2, peaks are closer to the frequency range (10 to 30 MHz) of interest but did not have that much influence on spectral slopes because their heights were relatively small. That is why the spectral slopes for the distributions Mixture1 and Mixture2 were slightly smaller than that of the Regular.

We found that the IBSC between 10 and 30 MHz increased by about 7 dB for the highest poly-disperse medium considered in this study compared with the mono-disperse sample. This is consistent with published experimental results. For example, in a recent paper, Vlad *et al.* [2] showed that for an AML cell pellet, the ultrasound integrated backscatter increased by nearly 7 dB after a radiotherapy treatment which induced cell death, causing an increased cell size variance. Furthermore, the spectral slope did not change significantly. In another experiment, Kolios *et al.* [1] measured an increase of 7 to 8 dB at 35 MHz for apoptotic AML cells after exposure to a drug (colchicine) compared with that of healthy cells, and the corresponding spectral slope increased by about 0.16 dB/MHz.

The model discussed here can incorporate the size dispersity of scatterers. Thus, it provides a realistic framework to compute ultrasound backscattering by a collection of particles with heterogeneous sizes. Moreover, it is valid over the entire frequency range because the exact analytical solution has been used to determine the single-particle backscattering amplitude. However, the exact solution can only be obtained for some regular shapes (sphere, cylinder, layer, etc.), and therefore (4) can be used only for situations where scatterers can be approximated as objects with regular shapes. In addition, computation of (4) is much more intensive than that of (5). For example, it took about 10 min for each simulation to compute (5) to obtain the BSC for a mono-disperse sample (Mono-disperse) on a remote computer cluster [operating system: Linux CentOS 5, RAM: 16 GB, processor: Intel Xenon E5462 Quad Core 2.8 GHz for each node (Intel Corp., Santa Clara, CA)]. The execution time was nearly 7 h for each simulation to evaluate (4) on the same computing platform for the highest poly-disperse sample (Poly-disperse2).

B. Backscatter Signal Results

Hunt *et al.* [11] found that backscatter signal corresponding to the central region of a sample similar to our first sample (labeled as Regular) was greatly reduced because of destructive interference for an input pulse with a 3.5 MHz center frequency. As the randomization increased, signal strength also increased in that region. We also observed similar trends for both the 5-MHz and 25-MHz incident pulses. Another interesting observation is that if the interrogating pulse contains a frequency for which wavelength and periodicity are related by $d \sim \lambda/2$, the signal statistics can be better described by the Nakagami distribution function. In this case, the corresponding SNR values were greater than 1.91 and the values for β were found to be greater than 1, confirming deviations of backscatter echo envelope histograms from the Rayleigh distribution [18]. We confirmed this effect up to the nuclei mixture in which 25.64% of the total nuclei were packed periodically and the remaining nuclei were randomly distributed. When the proportion of regularly arranged nuclei was less than 25%, this effect was smaller. The variation of histogram pattern with spatial organization of scatterers is in accordance with previous work by Shankar [18]. It was shown that the signal envelope histograms followed the Nakagami distribution for situations in which the sample contained unresolvable periodic alignment of scatterers in addition to a collection of randomly located scatterers. The later distributions can better capture the complex situations in which signals contain coherent components originating from periodically aligned scatterers.

On the other hand, it is shown that the signal envelope statistics followed the Rayleigh distribution although the samples contained poly-disperse scatterers. This was further confirmed from the fact that for these samples, β values from the Nakagami distribution were also computed to be close to 1. Thus, it may be inferred that at this level of packing (>7000 scatterers/mm^2) the spatial organization of particles played a more significant role on the shape of a signal envelope histogram than the scatterer size distribution. This might be because the signal envelope characteristics were primarily determined by the interference of backscatter signals generated by the individual scatterers which was governed by the phase relationships (originating from the spatial organization of scatterers) of those signals. The size distribution would only control the strength (backscattering amplitudes would be different for

different scatterers depending upon their sizes) of those signals and played a lesser role to their phase relationships than the spatial organization.

VI. Conclusions

A modeling approach pertinent to ultrasound backscattering by cell aggregates was presented. It was developed by drawing analogy with ultrasound backscattering by red blood cells. In cell aggregates (such as in tumors), cells are tightly packed and therefore it can be assumed that nuclei mainly act as scattering centers. The nuclei embedded in cytoplasm were treated as weak scatterers of ultrasound waves, and hence multiple scattering was neglected. The scattering pattern of each nucleus was assumed to be given by the exact analytical solution for the scattering of an incident plane wave by a fluid sphere. The resultant backscatter signal by a collection of particles was obtained by using the linear superposition of backscatter waves that originated from the nuclei. The theoretical model has been employed to examine spatial organization and size-distribution-dependent ultrasound backscattering by AML cells. A Monte Carlo simulation technique was implemented to generate 2-D tissue realizations, and consequently, both frequency-dependent BSCs and signal statistics were studied for different tissue configurations.

The present study confirms that the spatial organization of scatterers strongly influences ultrasound backscattering. The BSC increased as the sample contained more randomly distributed particles. It was estimated that the IBSC between 10 and 30 MHz increased by nearly 27 dB when the sample comprised a collection of randomly located scatterers instead of regularly aligned nuclei. The corresponding spectral slope diminished from 4.36 to 4.17. The IBSCs also increased in case of poly-disperse samples. An approximately 7 dB enhancement of IBSC was computed for the highest poly-dispersive medium compared with that of a mono-disperse sample. The associated spectral slope also increased from 4.17 to 4.47. Analysis of the signal envelope statistics revealed that for randomly positioned scatterers, the Rayleigh distribution function provided good fits to the envelope histograms for both mono-disperse and poly-disperse samples. However, for samples with partially ordered particles and if the irradiating pulse contained a frequency for which the wavelength became comparable to the scatterer spacing periodicity ($d \sim \lambda/2$), then the Nakagami distribution function provided better fits to the histograms. This study suggests that the shape of an envelope histogram depends upon the periodicity in the spatial organization of scatterers and bandwidth of the input pulse. The insights derived from this work are expected to help in the analysis of backscatter echoes from tumors using spectral and envelope statistics methods to quantify the portion of cells that respond to a treatment.

References

[1] M. C. Kolios, G. J. Czarnota, M. Lee, J. W. Hunt, and M. D. Sherar, "Ultrasonic spectral parameter characterization of apoptosis," *Ultrasound Med. Biol.*, vol. 28, no. 5, pp. 589–597, 2002.

[2] R. M. Vlad, N. M. Alajez, A. Giles, M. C. Kolios, and G. J. Czarnota, "Quantative ultrasound characterization of cancer radiotherapy effects in vitro," *Int. J. Radiat. Oncol. Biol. Phys.*, vol. 72, no. 4, pp. 1236–1243, 2008.

[3] A. S. Tunis, G. J. Czarnota, A. Giles, M. D. Sherar, J. W. Hunt, and M. C. Kolios, "Monitoring structural changes in cells with high frequency ultrasound signal statistics," *Ultrasound Med. Biol.*, vol. 31, no. 8, pp. 1041–1049, 2005.

[4] G. J. Czarnota, M. C. Kolios, J. Abraham, M. Portnoy, F. P. Ottensmeyer, J. W. Hunt, and M. D. Sherar, "Ultrasonic imaging of apoptosis: High-resolution non-invasive imaging of programmed cell death in vitro, in situ and in vivo," *Br. J. Cancer*, vol. 81, no. 3, pp. 520–527, 1999.

[5] G. J. Czarnota, M. C. Kolios, H. Vaziri, S. Benchimol, F. P. Ottensmeyer, M. D. Sherar, and J. W. Hunt, "Ultrasonic imaging of viable, dead and apoptotic cells," *Ultrasound Med. Biol.*, vol. 23, no. 6, pp. 961–965, 1997.

[6] F. G. Blankenberg, "In vivo detection of apoptosis," *J. Nucl. Med.*, vol. 49, suppl. 2, pp. 81S–95S, 2008.

[7] F. L. Lizzi, M. Greenbaum, E. J. Feleppa, M. Elbaum, and D. J. Coleman, "Theoretical framework for spectrum analysis in ultrasonic tissue characterization," *J. Acoust. Soc. Am.*, vol. 73, no. 4, pp. 1366–1373, 1983.

[8] M. L. Oelze, W. D. O'Brien Jr., J. P. Blue, and J. F. Zachary, "Differentiation and characterization of rat mammary fibroadenomas and 4T1 mouse carcinomas using quantitative ultrasound imaging," *IEEE Trans. Med. Imaging*, vol. 23, no. 6, pp. 764–771, 2004.

[9] M. F. Insana, R. F. Wagner, D. G. Brown, and T. J. Hall, "Describing small-scale structure in random media using pulse-echo ultrasound," *J. Acoust. Soc. Am.*, vol. 87, no. 1, pp. 179–192, 1990.

[10] M. L. Oelze and J. F. Zachary, "Examination of cancer in mouse models using high-frequency quantitative ultrasound," *Ultrasound Med. Biol.*, vol. 32, no. 11, pp. 1639–1648, 2006.

[11] J. W. Hunt, A. E. Worthington, and A. T. Kerr, "The subtleties of ultrasound images of an ensemble of cells: Simulation from regular and more random distributions of scatterers," *Ultrasound Med. Biol.*, vol. 21, no. 3, pp. 329–341, 1995.

[12] J. W. Hunt, A. E. Worthington, A. Xuan, M. C. Kolios, G. J. Czarnota, and M. D. Sherar, "A model based upon pseudo regular spacing of cells combined with the randomisation of the nuclei can explain the significant changes in high-frequency ultrasound signals during apoptosis," *Ultrasound Med. Biol.*, vol. 28, no. 2, pp. 217–226, 2002.

[13] K. K. Shung and G. A. Thieme, *Ultrasound Scattering in Biological Tissues.* Boca Raton, FL: CRC Press, 1993.

[14] D. Savéry and G. Cloutier, "Effect of red cell clustering and anisotropy on ultrasound blood backscatter: A Monte Carlo study," *IEEE Trans. Ultrason. Ferroelectr. Freq. Control*, vol. 52, no. 1, pp. 94–103, 2005.

[15] F. T. H. Yu and G. Cloutier, "Experimental ultrasound characterization of red blood cell aggregation using the structure factor size estimator (SFSE)," *J. Acoust. Soc. Am.*, vol. 122, no. 1, pp. 645–656, 2007.

[16] R. K. Saha and G. Cloutier, "Monte Carlo study on ultrasound backscattering by three-dimensional distributions of red blood cells," *Phys. Rev. E*, vol. 78, no. 6, art. no. 061919, 2008.

[17] R. M. Vlad, R. K. Saha, N. M. Alajez, S. Ranieri, G. J. Czarnota, and M. C. Kolios, "An increase in cellular size variance contributes to the increase in ultrasound backscatter during cell death," *Ultrasound Med. Biol.*, vol. 36, no. 9, pp. 1546–1558, 2010.

[18] P. M. Shankar, "A general statistical model for ultrasonic backscattering from tissues," *IEEE Trans. Ultrason. Ferroelectr. Freq. Control*, vol. 47, no. 3, pp. 727–736, 2000.

[19] B. I. Raju and M. A. Srinivasan, "Statistics of envelope of high-frequency ultrasonic backscatter from human skin in vivo," *IEEE Trans. Ultrason. Ferroelectr. Freq. Control*, vol. 49, no. 7, pp. 871–882, 2002.

[20] F. Destrempes and G. Cloutier, "A critical review and uniformized representation of statistical distributions modeling the ultrasound echo envelope," *Ultrasound Med. Biol.*, vol. 36, no. 7, pp. 1037–1051, 2010.

[21] P. M. Morse and K. U. Ingard, *Theoretical Acoustics.* New York, NY: McGraw-Hill, 1968, ch. 8.

[22] V. Twersky, "Low-frequency scattering by correlated distributions of randomly oriented particles," *J. Acoust. Soc. Am.*, vol. 81, no. 5, pp. 1609–1618, 1987.

[23] K. K. Shung, Y. W. Yuan, D. Y. Fei, and J. M. Tarbell, "Effect of flow disturbance on ultrasonic backscatter from blood," *J. Acoust. Soc. Am.*, vol. 75, no. 4, pp. 1265–1272, 1984.

[24] G. E. Sleefe and P. P. Lele, "Tissue characterization based on scatterer number density estimation," *IEEE Trans. Ultrason. Ferroelectr. Freq. Control*, vol. 35, no. 6, pp. 749–757, 1988.

[25] V. Dutt and J. F. Greenleaf, "Ultrasound echo envelope analysis using a homodyned K distribution signal model," *Ultrason. Imaging*, vol. 16, no. 4, pp. 265–287, 1994.

[26] R. K. Saha and S. K. Sharma, "Validity of a modified Born approximation for a pulsed plane wave in acoustic scattering problems," *Phys. Med. Biol.*, vol. 50, no. 12, pp. 2823–2836, 2005.

[27] P. M. Shankar, "Ultrasonic tissue characterization using a generalized Nakagami model," *IEEE Trans. Ultrason. Ferroelectr. Freq. Control*, vol. 48, no. 6, pp. 1716–1720, 2001.

[28] D. P. Hruska and M. L. Oelze, "Improved parameter estimates based on the homodyned K distibution," *IEEE Trans. Ultrason. Ferroelectr. Freq. Control*, vol. 56, no. 11, pp. 2471–2481, 2009.

[29] R. C. Waag, J. O. Nilsson, and J. P. Astheimer, "Characterization of volume scattering power spectra in isotropic media from power spectra of scattering by planes," *J. Acoust. Soc. Am.*, vol. 74, no. 5, pp. 1555–1571, 1983.

[30] L. R. Taggart, R. E. Baddour, A. Giles, G. J. Czarnota, and M. C. Kolios, "Ultrasonic characterization of whole cells and isolated nuclei," *Ultrasound Med. Biol.*, vol. 33, no. 3, pp. 389–401, 2007.

[31] E. L. Hinrichsen, J. Feder, and T. Jøssang, "Random packing of disks in two dimensions," *Phys. Rev. A*, vol. 41, no. 8, pp. 4199–4209, 1990.

[32] R. E. Baddour and M. C. Kolios, "The fluid and elastic nature of nucleated cells: Implications from the cellular backscatter response," *J. Acoust. Soc. Am.*, vol. 121, no. 1, pp. EL16–EL22, 2007.

[33] O. Falou, M. Rui, A. E. Kaffas, J. C. Kumaradas, and M. C. Kolios, "The measurement of ultrasound scattering from individual micronsized objects and its application in single cell scattering," *J. Acoust. Soc. Am.*, vol. 128, no. 2, pp. 894–902, 2010.

[34] E. L. Hinrichsen, J. Feder, and T. Jøssang, "Geometry of random sequential adsorption," *J. Stat. Phys.*, vol. 44, no. 5–6, pp. 793–827, 1986.

[35] M. I. Daoud and J. C. Lacefield, "Stochastic modeling of normal and tumor tissue microstructure for high-frequency ultrasound imaging simulations," *IEEE Trans. Biomed. Eng.*, vol. 56, no. 12, pp. 2806–2815, 2009.

[36] T. Aste, "Circle, sphere, and drop packing," *Phys. Rev. E*, vol. 53, no. 3, pp. 2571–2579, 1996.

[37] Olympus NDT Inc., (2009, Dec. 21) Panametrics Ultrasound Transducers: Wedges, Cables, Test Blocks. [Online]. Available: http://www.olympus-ims.com/data/File/panametrics/panametrics-UT.en.pdf

Ratan K. Saha was born at Alipurduar, West Bengal, India, in 1973. He completed his B.Sc. degree in physics from the ABN Seal College, University of North Bengal, West Bengal, in 1996. He received his M.Sc. degree in physics from the Jadavpur University, Kolkata, West Bengal, in 1999. In 2000, he joined the Saha Institute of Nuclear Physics, Kolkata, as a research fellow and obtained his Ph.D. degree from the West Bengal University of Technology, Kolkata, in 2007. He was associated as a postdoctoral fellow during 2007–2008 with the Laboratory of Biorheology and Medical Ultrasonics, University of Montreal Hospital Research Centre, Montréal, Québec, Canada. Currently, he is with the Department of Physics, Ryerson University, Toronto, Ontario, Canada, as a postdoctoral fellow. His research interests include ultrasonic and photoacoustic tissue characterizations using computer simulations.

Michael C. Kolios was born in Toronto, Canada, and moved to Greece at a young age, finishing his high school studies in Athens, Greece. He completed a B.Sc. Hons. degree in physics, with a computer science minor, at the University of Waterloo in 1991. He subsequently completed his M.Sc. and Ph.D. degrees in the Department of Medical Biophysics at the University of Toronto in 1994 and 1998, respectively. In 1997, he joined the Department of Physics at Ryerson University, where he is currently an associate professor and Program Director of the graduate program in Biomedical Physics. He holds a Canada Research Chair in Biomedical Applications of Ultrasound and has been the recipient of numerous awards for his research and teaching. His research interests include ultrasound/optical imaging and characterization of tissues and cells, high-frequency ultrasound imaging and spectroscopy, acoustic microscopy, ultrasound- and laser-based therapy, optical coherence tomography, and photoacoustic imaging. More information about his work can be found at http://www.physics.ryerson.ca/user/4